Inorganic Chemistry

Article

pubs.acs.org/IC

Room-Temperature Synthesis, Hydrothermal Recrystallization, and Properties of Metastable Stoichiometric FeSe

F. Nitsche,[†] T. Goltz,[‡] H.-H. Klauss,[‡] A. Isaeva,[†] U. Müller,[†] W. Schnelle,[§] P. Simon,[§] Th. Doert,*[,†] and M. Ruck[†,§]

[†]Department of Chemistry and Food Chemistry, Technische Universität Dresden, D-01062 Dresden, Germany

[‡]Institute of Solid State Physics, Technische Universität Dresden, D-01062 Dresden, Germany

[§]Max Planck Institute for Chemical Physics of Solids, D-01187 Dresden, Germany

Supporting Information

ABSTRACT: Room-temperature precipitation from aqueous solutions yields the hitherto unknown metastable stoichiometric iron selenide (ms-FeSe) with tetragonal anti-PbO type structure. Samples with improved crystallinity are obtained by diffusion-controlled precipitation or hydrothermal recrystallization. The relations of ms-FeSe to superconducting β-$FeSe_{1-x}$ and other neighbor phases of the iron−selenium system are established by high-temperature X-ray diffraction, DSC/TG/MS (differential scanning calorimetry/thermogravimetry/mass spectroscopy), ^{57}Fe Mössbauer spectroscopy, magnetization measurements, and transmission electron microscopy. Above 300 °C, ms-FeSe decomposes irreversibly to β-$FeSe_{1-x}$ and Fe_7Se_8. The structural parameters of ms-FeSe ($P4/nmm$, a = 377.90(1) pm, c = 551.11(3) pm, Z = 2), obtained by Rietveld refinement, differ significantly from literature data for β-$FeSe_{1-x}$. The Mössbauer spectrum rules out interstitial iron atoms or additional phases. Magnetization data suggest canted antiferromagnetism below T_N = 50 K. Stoichiometric non-superconducting ms-FeSe can be regarded as the true "parent" compound for the "11" iron-chalcogenide superconductors and may serve as starting point for new chemical modifications.

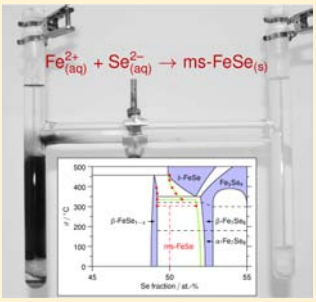

INTRODUCTION

Compounds containing square iron nets received new attention from physicists and chemists alike after the discovery of superconductivity up to 55 K in doped rare-earth iron pnictides.[1,2] Besides the search for new structures with potential for high-temperature superconductivity, a closer inspection of known compounds revealed superconducting properties. β-$FeSe_{1-x}$ with anti-PbO type structure[3] is one example.

Considerable research on the iron−selenide system has been performed, and the complex phase diagram is well established.[4] Tetragonal β-$FeSe_{1-x}$ was first reported by Hägg and Kindström[5] in 1933. It is found to undergo a peritectoid decomposition at 457 °C into α-Fe and δ-FeSe (NiAs type) and exhibits a narrow homogeneity range around 49 at. % Se (see Figure 4).[4,6] Hexagonal δ-FeSe is formed in an eutectoid reaction of δ-$FeSe_{1-x}$ and Fe_3Se_4 (defect NiAs type, see Table 1) at 350 °C. Although Fe_3Se_4- and Fe_7Se_8-type phases are nonstoichiometric compounds with vacancy-ordered structures and a considerable homogeneity range, we refer to them only as Fe_3Se_4 and Fe_7Se_8 for shortness and clarity.

Table 1. Overview of the Phases Discussed in the Text

designation	structure type	crystal system
β-$FeSe_{1-x}$	anti-PbO	tetragonal
ms-FeSe	anti-PbO	tetragonal
δ-FeSe	NiAs	hexagonal
Fe_3Se_4	defect-NiAs	orthorhombic
Fe_7Se_8 (α, β)	defect-NiAs	monoclinic

The structural background of the nonstoichiometry of β-$FeSe_{1-x}$ is still under debate: Either excess iron atoms occupy interstitial positions between the layers in analogy to Fe_2As,[7] or some of the selenium positions are void.[8,9] Whereas doping is needed for the iron pnictide phases (e.g., $BaFe_2As_2$ so-called "Ba-122" and LaFeAsO "La-1111")[10] to become superconducting, the intrinsic doping of β-$FeSe_{1-x}$ ("11") by deviation from the precise 1:1 composition induces superconductivity.[8,9,11] In contrast to the "122" and "1111" phases, substitution of iron by other transition metals leads to suppression or only small enhancement of superconductivity in iron selenide.[12−14]

Crystals of tetragonal β-$FeSe_{1-x}$ grown at temperatures above the peritectoid point are often pseudomorphic showing the hexagonal habitus of δ-FeSe.[15−19] Consequently, growth of single crystals has to be performed within the stability range of β-$FeSe_{1-x}$, as shown by Oyler et al.,[20] by the reaction of elemental precursors in high-boiling organic solvents.

For the sulfide FeS, a synthesis in aqueous media at room temperature has been reported.[21,22] Furthermore, theoretical studies of the solubility of iron chalcogenides in water have been performed.[23] The synthesis of FeSe in water is feasible only in the absence of oxygen, since the product[11] and the

Received: April 18, 2012
Published: June 20, 2012

dx.doi.org/10.1021/ic300798p | Inorg. Chem. 2012, 51, 7370−7376

reactants are easily oxidized. Following these ideas, we conducted a diffusion-controlled precipitation from aqueous solutions and obtained metastable FeSe (ms-FeSe) with anti-PbO type structure and stoichiometric 1:1 composition. It represents the undoped non-superconducting "parent" compound for the "11" system and provides a starting point for future chemical modifications, to induce superconductivity in analogy to the "122" and "1111" systems.

We report on the synthesis and hydrothermal recrystallization of ms-FeSe. The relation of ms-FeSe to the neighbor phases of the Fe−Se system is investigated and discussed. Finally, the crystal structure data, the Mössbauer spectrum, and the magnetic and thermal properties are given.

EXPERIMENTAL SECTION

All starting materials and products are oxygen-sensitive and were handled and stored in an argon-filled glovebox (M. Braun; $p(O_2)/p_0 \leq 1$ ppm, $p(H_2O)/p_0 \leq 1$ ppm, argon purified with molecular sieve and copper catalyst).

Starting Materials. Li_2Se was prepared by reacting lithium (>99%, Acros Organics) and selenium (99.999%, Chempur, treated with H_2 at 150 °C) under Schlenk conditions in freshly dried tetrahydrofuran (THF, 99.7%, VWR) using naphthalene (99%, Acros Organics) as catalyst.[24] The obtained creme-colored solid was washed three times with THF and dried under vacuum.

FeI_2 was prepared by the reaction of the elements (Fe: 99.5%, Alfa Aeser; I_2: >99.8%, Merck, sublimated twice over BaO) in a silica ampule (15 cm length, 14 mm diameter) using 10 at. % excess of iron. The iron-containing side of the ampule was placed in a horizontal tube furnace at 550 °C, while the other side of the ampule resided outside the furnace to limit the pressure of gaseous iodine. FeI_2 exhibits a noticeable vapor pressure at 550 °C[25] and was separated from the excess iron by sublimation.

Both starting materials are easily oxidized by molecular oxygen, yet they are stable and soluble in oxygen-free water. Thus, the water used for reactions was distilled under streaming argon to remove molecular oxygen (denoted as distilled water in the following text). Aqueous solutions of Li_2Se and FeI_2 are deep red and light green, respectively. Combining both liquids immediately yields a black precipitate which is amorphous according to X-ray diffraction.

Diffusion-Controlled Precipitation. An H-shaped tube was used for the controlled precipitation of ms-FeSe (Figure 1). Under argon, Li_2Se and FeI_2 powders were filled separately in the legs of the tube. To hinder uncontrolled dissolution and mixing of the reactants, silica wool was placed on top of the powders. Distilled water was added as diffusion medium and the tube was plugged. After 40 days at room temperature, a black precipitate had formed, which was then removed from the tube and washed three times with distilled water and dried subsequently under vacuum.

Hydrothermal Recrystallization. FeI_2 and Li_2Se were dissolved separately in distilled water in Schlenk tubes, and the solutions were combined in a silica tube. The resulting aqueous solution with the immediately formed black precipitate was frozen by immersing the container in liquid nitrogen before the open end was fused. The approximately half-filled ampule was inserted into a Teflon-lined steel autoclave (DAB-2, BERGHOF), which was then also half filled with water to generate the necessary counter-pressure for the ampule. The steel autoclave was stored in a heat-cabinet at 200 °C. After three days, the ampule was opened under argon in a glovebag (ABCR). The colorless solution was decanted, and the black polycrystalline material was washed three times with distilled water and dried subsequently under vacuum.

Characterization. Powder X-ray diffraction (PXRD) patterns at room temperature were measured with an X'Pert PRO diffractometer (PANalytical, Cu $K\alpha_1$, Ge monochromator, PIXcel detector), while high-temperature measurements (HT-PXRD) were performed on a Stadi P diffractometer (STOE, Cu $K\alpha_1$, Ge monochromator, linear position sensitive detector). The samples were enclosed in borosilicate or silica capillaries (Hilgenberg) for room- and high-temperature measurements, respectively. The temperature in the heating chamber for PXRD was calibrated by the melting points of Sn (232 °C, 99.99%, Fluka) and Zn (420 °C, 99.999%, Strem Chemicals). In the high-temperature experiment the temperature of measurement was accessed with a rate of 10 K min^{-1} and then kept constant while two powder diffraction patterns were taken subsequently with a measurement time of three hours each.

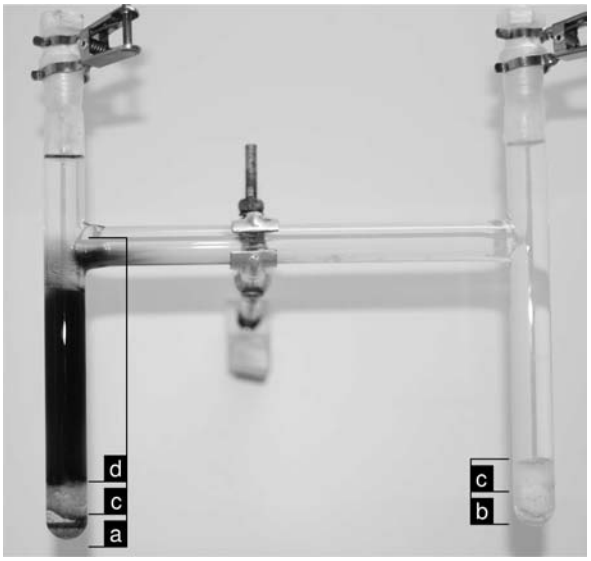

Figure 1. H-tube for diffusion-controlled reaction of Li_2Se (a) with FeI_2 (b) to ms-FeSe (d) with silica wool (c) inserted to prevent reactants from uncontrolled mixing during filling with distilled water. Photograph taken after 10 days of reaction.

Lattice parameters and phase fractions were obtained by Rietveld refinement using GSAS,[26] EXPGUI[27], and Jana2006,[28] applying models for axial divergence and anisotropic line broadening. Background contributions were fitted by Legendre polynomials. Absorption corrections for cylindrical samples corresponding to a packing of 60 vol. % in the 0.2 mm capillaries were applied. δ-FeSe, Fe_3Se_4, α-Fe_7Se_8, and β-Fe_7Se_8 were treated within NiAs-type models, since reflection splitting of the defect-NiAs type structures could not be observed due to the broad reflections. Nevertheless, differences in lattice parameters allow to distinguish the monoclinic phases (Fe_7Se_8) from δ-FeSe during cooling from high temperature.

The Fe/Se ratio of the sample was determined with an ICP-OES Vista RL (Varian) by previously dissolving the samples in a mixture of hydrochloric and nitric acid. The reported ratio is the average of three measurements from one sample.

Transmission electron microscopy (TEM) images at the middle resolution regime, as well as electron diffraction patterns, were recorded using a FEI Tecnai 10 microscope (LaB_6-source, 100 kV, TEM camera TVIPS F224HD 2k × 2k). The images were analyzed using Digital Micrograph[29] and ImageJ.[30]

Differential scanning calorimetry measurements (DSC) combined with thermogravimetry (TG) and mass spectroscopy (MS) were performed with a STA 409 CD Skimmer (NETZSCH) operated inside a glovebox with high-purity argon.[31] Alumina-lined Pt-crucibles with lid were used and double runs with heating rates of 5 and 10 K min^{-1} were conducted. Baseline contributions were fitted with quadratic interpolation and subtracted.

^{57}Fe Mössbauer spectra were measured in transmission geometry at room temperature using a ^{57}Co/Rh γ-radiation source (emission line half width at half-maximum Γ = 0.135(2) mm s^{-1}) and a Kr/CO_2 proportional counter as detector. The spectrometer was calibrated to α-Fe at room temperature.

Full-potential linearized augmented plane-wave method (FP-LAPW) and basis sets implemented within the Elk code[32] were utilized for quantum chemical calculations. The generalized gradient

dx.doi.org/10.1021/ic300798p | Inorg. Chem. 2012, 51, 7370−7376

approximation (GGA) was employed for the exchange-correlation functional as proposed by Perdew and Wang.[33] A number of 90 irreducible k-points was considered. The electric field gradient (EFG) was computed from the converged self-consistent field (SCF) energy taking spin−orbit coupling into account. The constant magnetic field of 1.7 T was applied in the z-direction in order to break spin symmetry. The basis set was expanded with a number of FP-LAPW basis functions up to R_{MT} K_{max} = 12 (where R_{MT} is the average radius of the muffin-tin spheres and K_{max} is the maximum value of the wave vector $K = k + G$) and the maximum length of G for expanding the interstitial density and potential is equal to 22. The atomic orbitals up to an angular momentum l = 12 were used to expand the wave functions inside the muffin-tin spheres.

Magnetic measurement were performed with a SQUID-magnetometer (Quantum Design MPMS-XL7) in the temperature range between 1.8 and 400 K and external fields of 2 mT to 7 T. Samples were prepared in an argon-filled glovebox, transferred under argon, and measured in helium atmosphere. The susceptibility of the silica sample holder was determined prior to the measurement and subtracted.

RESULTS AND DISCUSSION

Diffusion-controlled room-temperature precipitation from aqueous solutions yielded tetragonal ms-FeSe according to the following equation:

$$FeI_{2(s)} + Li_2Se_{(s)} \xrightarrow{H_2O} \text{ms-FeSe}_{(s)} + 2Li^+_{(aq)} + 2I^-_{(aq)} \quad (1)$$

No additional phases were detected by powder X-ray diffraction. Preliminary HT-XRD and TG/MS investigations showed decomposition of the phase above 303(5) °C to Fe_3Se_4 and β-$FeSe_{1-x}$. MS showed only loss of residual solvent water but no selenium containing species.

Based on these results, a faster synthesis route was developed. The black precipitate obtained by fast mixing of solutions of Li_2Se and FeI_2 appears to be amorphous in PXRD. Hydrothermal treatment at 200 °C increases the crystallinity and yields ms-FeSe within three days instead of 40 days of the diffusion-controlled reaction. All further characterization was done with this sample.

Rietveld refinement of PXRD data of ms-FeSe (Figure 2) succeeded with a model for anisotropic particle size. Applying the Scherrer equation to the profile parameters leads to a particle size of 16 nm in c direction and 27 nm in the directions of the basal plane (further data in the Supporting Information).

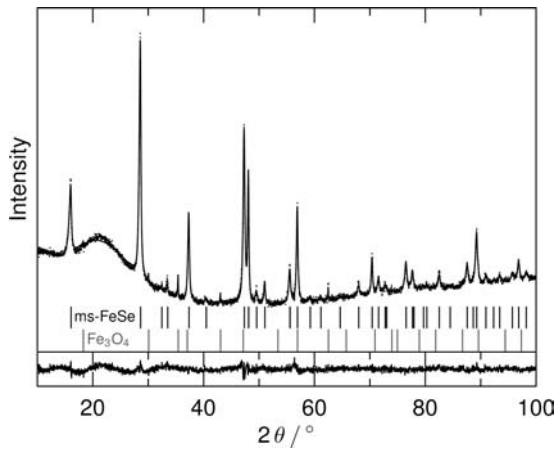

Figure 2. Rietveld refinement of ms-FeSe with 0.4(1) wt % magnetite impurity. Experimental data plotted as dots, fitted pattern as solid line. Lower panel: difference plot.

Magnetite, identified as an impurity phase with 0.4(1) wt % during Rietveld refinement, is believed to bias only the magnetic characterization.

ms-FeSe, as well as β-$FeSe_{1-x}$, crystallizes in the anti-PbO type structure. However, there are subtle yet significant differences (see Table 2): The c-axis of ms-FeSe is shorter

Table 2. Structure Data of ms-FeSe and β-$FeSe_{1-x}$[36,a]

param.	ms-FeSe	β-$FeSe_{1-x}$
a (pm)	377.90(1)	377.376(2)
c (pm)	551.11(3)	552.482(5)
c/a	1.45835(9)	1.46401(2)
z_{Se}	0.2655(3)	0.2652(1)
Fe−Se (pm)	239.0(1)	238.89(3)
Fe−Se−Fe (deg)	104.48(5)	104.34(1)
Se···Se_{vdW} (pm)	371.7(2)	372.18(5)

[a]both: space group $P4/nmm$, no. 129, 1st setting.

and the a-axis is longer than for β-$FeSe_{1-x}$,[5,8,11,17,34−38] resulting in a significantly smaller c/a ratio. In contrast, the distance of iron and selenium is equal. Consequently, the structural difference of ms-FeSe relative to β-$FeSe_{1-x}$ can be interpreted as an in-plane expansion of the iron−selenium slab accompanied by a contraction in stacking direction. The "tetrahedral" angle (Fe−Se−Fe in Table 2) increases correspondingly.

Plate-shaped crystals of ms-FeSe with broad particle-size distribution around 100 nm are identified by TEM (Figure 3). Electron diffraction patterns of isolated particles could be indexed with the tetragonal structure model of FeSe (Table 2). The major faces are {0 0 1} and the side faces belong to the form {1 1 0}. The preferred growth directions of ms-FeSe, thus, are ⟨1 0 0⟩. The observed anisotropy of the crystals supports the model used for Rietveld refinement.

While dissolving the samples for elemental analysis, some residual material remained. However, the determined ratio of iron and selenium gave 49.8(2) at. % Se, which is in excellent agreement with the 1:1 composition expected for a precipitation following eq 1. To further probe the composition of ms-FeSe, the relation to the phases in the literature-known phase diagram (Figure 4) was assessed by HT-PXRD and thermal analysis.

DSC experiments with ms-FeSe gave very similar results for different heating rates (5 and 10 K min^{-1}). However, the second heating of the sample differs markedly from the first (Figure 5), indicating that the sample is out of thermodynamic equilibrium before the first run. The second heating run can be interpreted based on the phase diagram given in Figure 4. The first endothermic signal corresponds to the eutectoid reaction of β-$FeSe_{1-x}$, Fe_3Se_4, and δ-FeSe at 332(2) °C. The symmetrical signal of the eutectoid reaction is invariant to the heating rate and superimposed with an asymmetrical signal, which corresponds to the solvus line of δ-FeSe ending at 441(1)°C and 50 at. % Se (extrapolation to zero heating rate) in agreement with the data reported by Katsuyama et al.[6] Consequently, the first heating run can be interpreted as an exothermal decomposition of ms-FeSe with 1:1 composition starting above 300 °C with the superimposed eutectoid reaction approaching the equilibrium evolution above 430 °C.

The HT-PXRD shows that the decomposition of ms-FeSe is starting at a kinetical temperature of 303(5) °C. Whereas the first HT-PXRD pattern at this temperature indicates only ms-

dx.doi.org/10.1021/ic300798p | Inorg. Chem. 2012, 51, 7370−7376

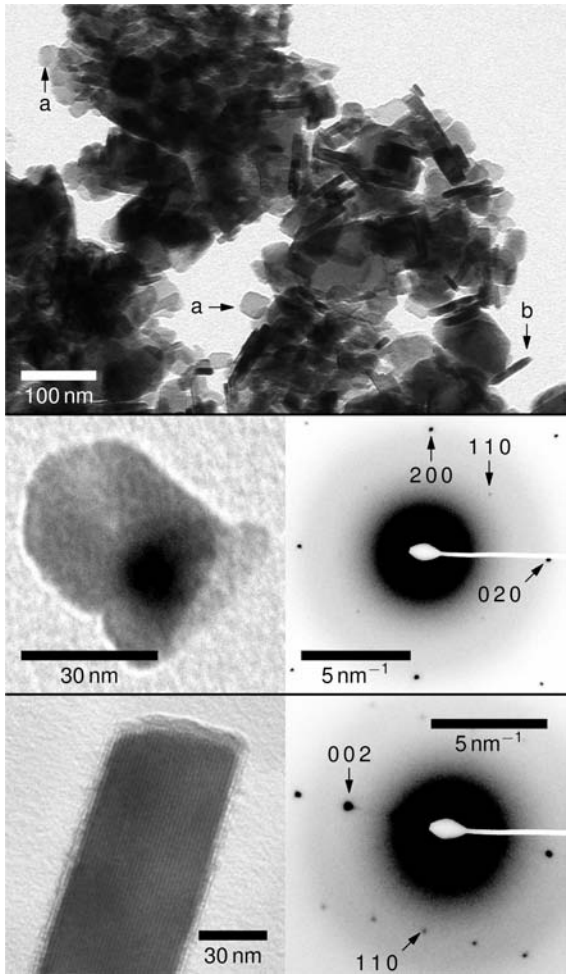

Figure 3. TEM images of ms-FeSe. Upper panel: overview, showing the particle-size distribution. (a) Plate-shaped crystallites oriented along the basal plane. (b) Crystallites with basal plane perpendicular to viewing direction. Middle panel: view along [0 0 1]. Lower panel: view along [1 $\bar{1}$ 0].

FeSe (point 1 in Figure 6), the second pattern, taken at the same temperature three hours later, shows a mixture of β-$FeSe_{1-x}$ and a NiAs type phase (point 2). Upon further heating,

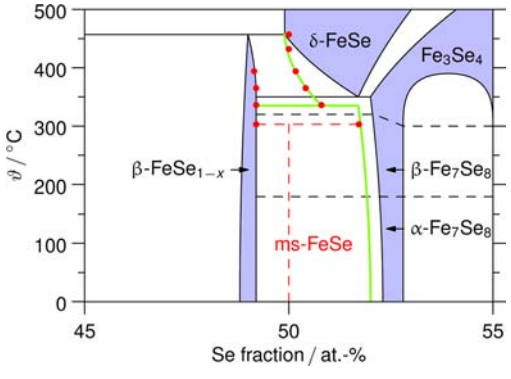

Figure 4. Phase diagram of iron and selenium in analogy to refs 4 and 6. Red points correspond to the results of Rietveld refinements of HT-PXRD data with the resulting solvus and eutectoid lines in green. Though ms-FeSe is not a thermodynamically stable phase, it is included in the phase diagram in order to visualize the relation of the compound to the neighbor phases.

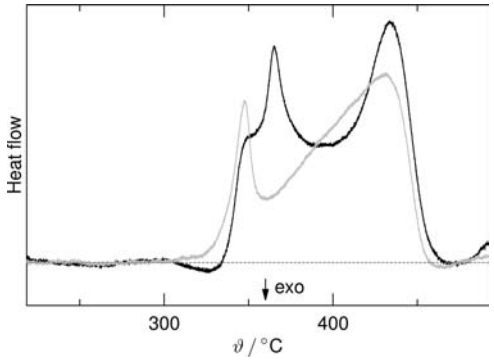

Figure 5. DSC measurement of ms-FeSe with a heating rate of 5 K min^{-1}. The black curve indicates the first heating run and the gray one the second. Dotted line marks zero.

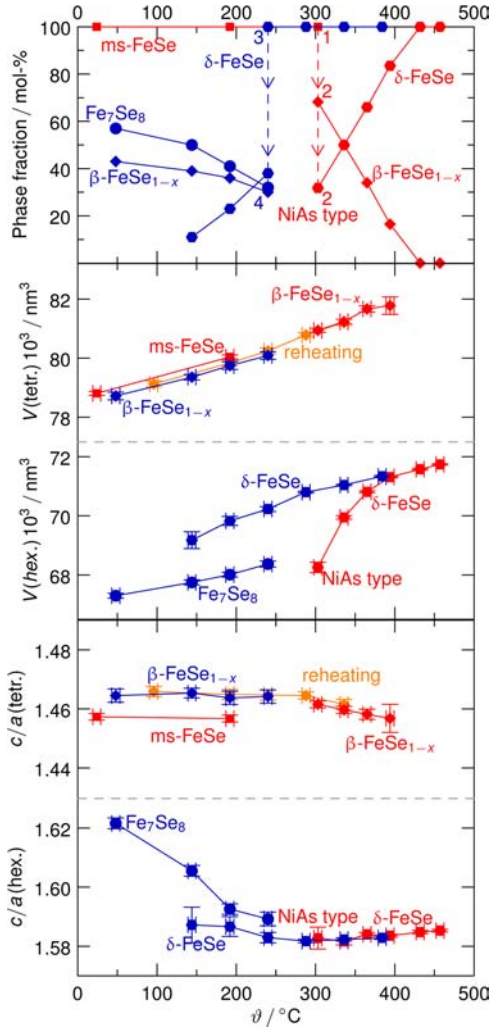

Figure 6. Evolution of phases and their lattice parameters as derived from Rietveld refinements. Red markers indicate the first heating run, blue markers the subsequent cooling, and orange markers the second heating run. Hexagons and circles indicate NiAs structure related phases. Diamonds indicate β-$FeSe_{1-x}$, and squares ms-FeSe. Points 1 and 2 are subsequent observations in the course of heating; points 3 and 4 are during cooling. Error bars represent the confidence interval of $\pm 2\sigma$ and are within markers in case of phase fractions. Lines are guides for the eye.

dx.doi.org/10.1021/ic300798p | Inorg. Chem. 2012, 51, 7370−7376

the content of the NiAs type phase increases following the solvus line in the phase diagram (Figure 4). HT-PXRD at 432(5) °C reveals that the sample has transformed completely into δ-FeSe, which corresponds well to the temperature of the solvus line of δ-FeSe at 50 at. % Se.

For temperatures above the decomposition of metastable ms-FeSe, the system is in equilibrium. The phase fractions determined by HT-PXRD can thus be transferred into the phase diagram (red markers in Figure 4) by applying the lever rule with the prerequisite of 49.2 at. % Se as the solvus line for β-$FeSe_{1-x}$. The so-obtained phase relations (green lines in Figure 4) follow tentatively the literature-known phase diagram with a slightly lower temperature for the eutectoid reaction and a different progression of the solvus line.

In summary, HT-PXRD and DSC measurements support the 1:1 composition obtained for ms-FeSe from elemental analysis. Furthermore, ms-FeSe and β-$FeSe_{1-x}$ can be distinguished by their unit cell volumes and c/a ratios (Table 2).

Upon cooling from 460 °C, δ-FeSe was supercooled down to 240(5) °C. The almost linear decrease of volume indicates constant composition (Figure 6). At 240 °C, the first HT-PXRD pattern shows δ-FeSe only (point 3 in Figure 6), while the subsequent HT-PXRD pattern indicates the beginning decomposition into β-$FeSe_{1-x}$ and Fe_7Se_8 (points 4). The formation of tetragonal β-$FeSe_{1-x}$ below 300 °C and its increasing phase fraction is in agreement with previous studies,[4] and suggests that the nonstoichiometric β-$FeSe_{1-x}$ is a thermodynamically stable phase at room temperature. These results refute the phase diagramm given by McQueen et al.[8] with tetragonal β-$FeSe_{1-x}$ as a high-temperature modification of hexagonal δ-FeSe above 300 °C.

While reheating the obtained phase mixture of β-$FeSe_{1-x}$, δ-FeSe, and Fe_7Se_8 (orange markers in Figure 6) the volume and c/a ratio of β-$FeSe_{1-x}$ coincide with the data of the first heating, indicating that the high-temperature behavior is reproducible. The pronounced decrease of the c/a ratio above 300 °C indicates a structural change of β-$FeSe_{1-x}$ beyond thermal expansion. To emphasize the effect, the linear thermal expansion coefficients $\alpha_a \approx \alpha_c \approx 3 \times 10^{-5}$ K were determined by linear regression based on the lattice parameters obtained for cooling and second heating in the range from room temperature to 250 °C. These coefficients are in good agreement with literature data for $Fe_{1.06}Te$ and $FeTe_{0.5}Se_{0.5}$.[39] After subtraction of the linear thermal expansion according to

$$a'(\vartheta) = a(\vartheta) - \alpha_a(\vartheta - 20°C)$$

(and correspondingly for c), the divergence of the a- and c-axes above 300 °C is discernible (Figure 7), emphasizing a structural change of β-$FeSe_{1-x}$ beyond thermal expansion. This effect can either be attributed to a structural reorganization (e.g., from selenium vacancies to iron interstitials) or a change of composition. It could, in any case, explain the influence of thermal treatment on the superconducting phase transition for various samples.[9,11,40]

Since the crystal structures of ms-FeSe and β-$FeSe_{1-x}$ differ in detail, small differences of the physical properties can be expected. The room-temperature Mössbauer spectrum (Figure 8) consists of an asymmetric doublet related to ms-FeSe. No sign of the Fe_3O_4 impurity was detected. From the spectrum, an isomer shift of δ = 0.43(1) mm s^{-1} and a quadrupole splitting of ΔE_Q = 0.28(1) mm s^{-1} is obtained for ms-FeSe (β-$FeSe_{1-x}$: δ = 0.45−0.47 mm s^{-1}, ΔE_Q = 0.26−0.29 mm s^{-1}).[7,8,38,41] While the quadrupole splitting is comparable for both phases,

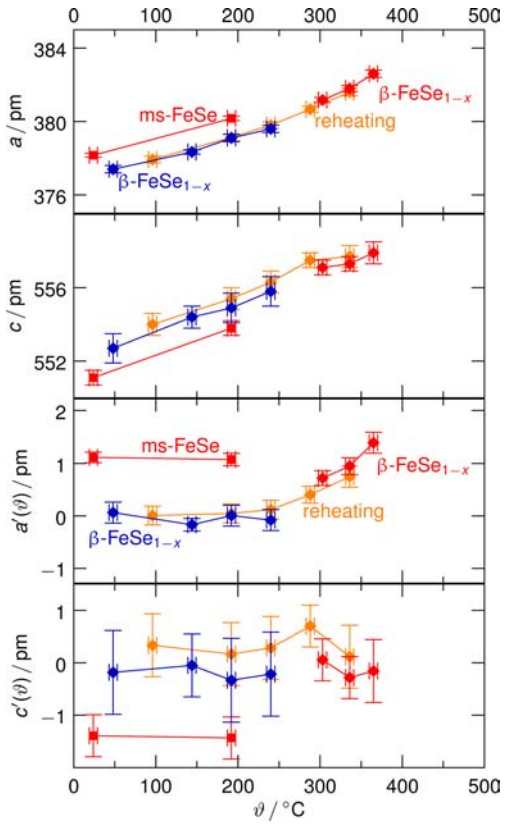

Figure 7. Temperature dependence of the lattice parameters of ms-FeSe and β-$FeSe_{1-x}$. The data in the two lower panels are corrected for thermal expansion. Red symbols indicate the first heating, blue symbols the cooling, and orange symbols the second heating run. Diamonds indicate β-$FeSe_{1-x}$, squares ms-FeSe. Error bars represent ±2σ. Lines are guides for the eye.

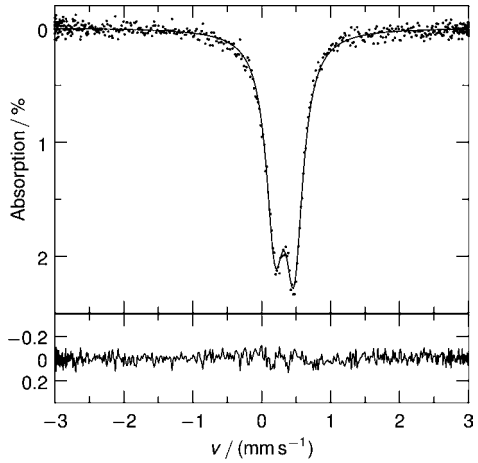

Figure 8. Mössbauer spectrum of ms-FeSe at room temperature. Experimental data plotted as dots, fitted doublet as solid line. Lower panel: difference plot.

the isomer shift in ms-FeSe is slightly smaller. This reflects an increase of the local electron density at the iron atoms as it would be expected for an itinerant system with a smaller c-axis (Table 2).

The asymmetry of the doublet pattern for ms-FeSe shows increased absorption at higher velocities. In contrast, Mössbauer spectra of β-$FeSe_{1-x}$ and $Fe_{1+x}Te$ show increased absorption at lower velocities, which has been attributed to

dx.doi.org/10.1021/ic300798p | Inorg. Chem. 2012, 51, 7370−7376

either occupation of interstitial sites by iron atoms or preferred orientation of the polycrystalline material (texture effect).[42−44] Following this argumentation, we can rule out interstitial iron atoms for ms-FeSe for two reasons: First, the asymmetry is opposite to experimental findings in all nonstochiometric samples. Second, assuming interstitial sites would lead to more than 2% off-stochiometry which is not consistent with the results from HT-PXRD, DSC, and elemental analysis.

The asymmetry can, however, be explained by preferred orientation. The plate-shaped particles (Figure 3) tend to orientate preferably with their basal plane parallel to the flatbed sample holder. In an ideal powder without preferred orientation, the vector of the principal axis v_{zz} of the electrical field gradient of the individual particle and the wavevector of the incident γ-radiation enclose in average the "magic angle" of 54.7° resulting in two symmetric absorption lines with equal intensity. A preferred orientation of the particles will lead to a deviation of this average angle ($\theta_{\gamma, Q}$) from the "magic angle", and thus to a change in the relative line intensities. With $v_{zz} > 0$, obtained from quantum chemical calculations, one finds $\theta_{\gamma,Q} = 50(2)°$ showing the presence of a preferred orientation consistent with plate-shaped particles.

Preliminary magnetic measurements of ms-FeSe in various external fields (Figure 9) indicate a ferro-like signal around 50

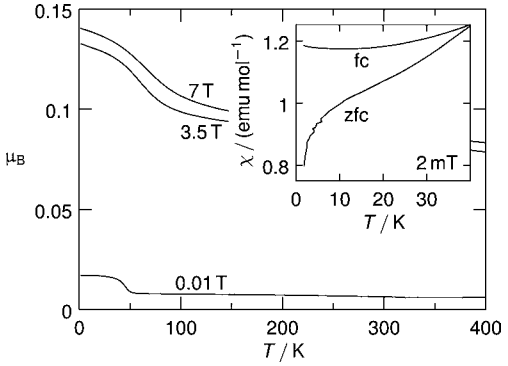

Figure 9. Temperature dependence of the magnetization of ms-FeSe in various external fields. Inset: Zero-field cooled (zfc) and field cooled (fc) magnetization measurement after thermal treatment of ms-FeSe up to 500 °C.

K, which saturates above 3.5 T. The very low moment of 0.03 μ_B per formula unit indicates a weak ordering which could be due to a canted antiferromagnetic state. It has to be noted that this may not necessarily reflect the bulk properties of ms-FeSe due to the small particle size. The ferrimagnetic magnetite impurity leads to a field dependency of the signal in the whole temperature range up to 400 K, hampering the interpretation of the measurement.

It is, however, evident that ms-FeSe is not superconducting down to 1.8 K in an external field of 2 mT. After thermal treatment up to 500 °C ms-FeSe has decomposed into the thermodynamically stable phases and magnetization indicates superconductivity below 10 K originating from β-$FeSe_{1-x}$ (Figure 9, inset). The increase of χ (with increasing temperature) from large positive values at 1.8 K after zero-field cooling (zfc) is due to spin freezing. It might also be explained by the additional phases δ-FeSe and Fe_7Se_8 (see phase fractions in Figure 6), which contribute to the overall susceptibility. Similar observations have also been made for other superconducting β-$FeSe_{1-x}$ samples.[9,15,37,45,46]

CONCLUSION

Precipitation from aqueous solutions of FeI_2 and Li_2Se yielded the yet unknown metastable phase ms-FeSe which has stoichiometric composition and anti-PbO type structure. It possibly exhibits magnetic ordering below 50 K and is nonsuperconducting down to 1.8 K in an external field of 2 mT. Above 300 °C, ms-FeSe decomposes irreversibly into the thermodynamically stable phases Fe_7Se_8 and β-$FeSe_{1-x}$.

ms-FeSe reveals a significantly shorter c and longer a-axis compared to β-$FeSe_{1-x}$, while the site parameter z for selenium is unchanged. As a consequence of the different local environment of iron relative to β-$FeSe_{1-x}$, the isomer shift in the Mössbauer spectrum is smaller. The difference of the line intensities of the doublet is attributed to texture effects due to preferred orientation of the crystallites.

There is evidence that β-$FeSe_{1-x}$ undergoes a structural change above 300 °C, which may be due to a change of composition or to a reorganization form interstitial iron atoms to selenium defects. This may explain the dependence of superconductivity on thermal treatment as pointed out by McQueen et al.[8] In contrast to recent reports,[8] β-$FeSe_{1-x}$ proves to be a thermodynamically stable phase at room-temperature.

Metastable stoichiometric ms-FeSe is the undoped "parent" compound for the tetragonal iron−selenium ("11") phases and thus opens up new ways for future chemical modifications in analogy to the "122" and "1111" systems. Substitution of iron with cobalt in the structure may lead to enhanced superconductivity and new properties, providing additional means to study the "simplest" system of iron-based superconductors.

ASSOCIATED CONTENT

Supporting Information

Detailed data of the Rietveld refinement of ms-FeSe (PDF) and corresponding crystallographic information file (CIF). This material is available free of charge via the Internet at http://pubs.acs.org/.

AUTHOR INFORMATION

Corresponding Author

*Email: thomas.doert@chemie.tu-dresden.de.

Notes

The authors declare no competing financial interest.

ACKNOWLEDGMENTS

The authors like to thank Prof. Dr. Peer Schmidt and Mr. Philipp Materne for discussions, Dr. Stefan Hoffmann and Susann Scharsach for thermal analysis, Dr. Gudrun Auffermann for elemental analysis, and Ms. Gudrun Kadner for experimental help. Part of this work was financially supported by the German Research Foundation (DFG) within the priority program SPP1458, project KL-1086/10-1.

REFERENCES

(1) Kamihara, Y.; Watanabe, T.; Hirano, M.; Hosono, H. *J. Am. Chem. Soc.* **2008**, *130*, 3296−3297.

(2) Ren, Z.-A.; Che, G.-C.; Dong, X.-L.; Yang, J.; Lu, W.; Yi, W.; Shen, X.-L.; Li, Z.-C.; Sun, L.-L.; Zhou, F.; Zhao, Z.-X. *EPL (Europhys. Lett.)* **2008**, *83*, 17002.

(3) Hsu, F.; Luo, J.; Yeh, K.; Chen, T.; Huang, T.; Wu, P. M.; Lee, Y.; Huang, Y.; Chu, Y.; Yan, D.; Wu, M. *Proc. Natl. Acad. Sci. U.S.A.* **2008**, *105*, 14262−14264.

(4) Okamoto, H. *J. Phase Equilib.* **1991**, *12*, 383−389.

(5) Hägg, G.; Kindström, A. *Z. Phys. Chem.* **1933**, *B22*, 453−464.
(6) Katsuyama, S.; Ueda, Y.; Kosuge, K. *Mater. Res. Bull.* **1990**, *25*, 913−922.
(7) Tsuji, T.; Howe, A. T.; Greenwood, N. N. *J. Solid State Chem.* **1976**, *17*, 157−163.
(8) McQueen, T. M.; Huang, Q.; Ksenofontov, V.; Felser, C.; Xu, Q.; Zandbergen, H.; Hor, Y. S.; Allred, J.; Williams, A. J.; Qu, D.; Checkelsky, J.; Ong, N. P.; Cava, R. J. *Phys. Rev. B* **2009**, *79*, 014522.
(9) Williams, A. J.; McQueen, T. M.; Cava, R. J. *Solid State Commun.* **2009**, *149*, 1507−1509.
(10) Paglione, J.; Greene, R. L. *Nat. Phys.* **2010**, *6*, 645−658.
(11) Pomjakushina, E.; Conder, K.; Pomjakushin, V.; Bendele, M.; Khasanov, R. *Phys. Rev. B* **2009**, *80*, 024517.
(12) Wu, M. K.; et al. *Phys. C* **2009**, *469*, 340−349.
(13) Thomas, E. L.; Wong-Ng, W.; Phelan, D.; Millican, J. N. *J. Appl. Phys.* **2009**, *105*, 073906.
(14) Mizuguchi, Y.; Tomioka, F.; Tsuda, S.; Yamaguchi, T.; Takano, Y. *J. Phys. Soc. Jpn.* **2009**, *78*, 074712.
(15) Zhang, S. B.; Sun, Y. P.; Zhu, X. D.; Zhu, X. B.; Wang, B. S.; Li, G.; Lei, H. C.; Luo, X.; Yang, Z. R.; Song, W. H.; Dai, J. M. *Supercond. Sci. Technol.* **2009**, *22*, 015020.
(16) Patel, U.; Hua, J.; Yu, S. H.; Avci, S.; Xiao, Z. L.; Claus, H.; Schlueter, J.; Vlasko-Vlasov, V. V.; Welp, U.; Kwok, W. K. *Appl. Phys. Lett.* **2009**, *94*, 082508.
(17) Mok, B. H.; Rao, S. M.; Ling, M. C.; Wang, K. J.; Ke, C. T.; Wu, P. M.; Chen, C. L.; Hsu, F. C.; Huang, T. W.; Luo, J. Y.; Yan, D. C.; Ye, K. W.; Wu, T. B.; Chang, A. M.; Wu, M. K. *Cryst. Growth Des.* **2009**, *9*, 3260−3264.
(18) Takeya, H.; Kasahara, S.; Hirata, K.; Mochiku, T.; Sato, A.; Takano, Y. *Phys. C* **2010**, *470* (Supplement1), S497−S498.
(19) Hara, Y.; Takase, K.; Yamasaki, A.; Sato, H.; Miyakawa, N.; Umeyama, N.; Ikeda, S. *Phys. C* **2010**, *470* (Supplement 1), S313−S314.
(20) Oyler, K. D.; Ke, X.; Sines, I. T.; Schiffer, P.; Schaak, R. E. *Chem. Mater.* **2009**, *21*, 3655−3661.
(21) Berner, R. A. *J. Geol.* **1964**, *72*, 293−306.
(22) Lennie, A. R.; Redfern, S. A. T.; Schofield, P. F.; Vaughan, D. J. *Mineral. Mag.* **1995**, *59*, 677−683.
(23) Makarov, G. V.; Voevoda, N. Y.; Batrakov, V. V.; Kudasheva, T. V. *Zh. Fiz. Khim.* **1993**, *67*, 1573−1576.
(24) Thompson, D. P.; Boudjouk, P. *J. Org. Chem.* **1988**, *53*, 2109−2112.
(25) Knacke, O.; Kubaschewski, O. In *Thermochemical Properties of Inorganic Substances*, 2nd ed.; Hesselmann, K., Ed.; Springer-Verlag: Germany, 1991; Vol. *1*−*2*.
(26) Larson, A. C.; Von Dreele, R. B. *Los Alamos National Labratory Report*; Los Alamos National Laboratory: Los Alamos, NM, 2000; pp 86−748.
(27) Toby, B. H. *J. Appl. Crystallogr.* **2001**, *34*, 210−213.
(28) Petricek, V.; Dusek, M.; Palatinus, L. *Jana2006*; Institute of Physics: Praha, Czech Republic, 2006.
(29) *Digital Micrograph*; Gatan Inc.: Pleasanton, CA, 2003.
(30) Abramoff, M. D.; Magelhaes, P. J.; Ram, S. J. *Biophotonics Int.* **2004**, *11*, 36−42.
(31) Hoffmann, S.; Schmidt, M.; Scharsach, S.; Kniep, R. *Thermochim. Acta* **2012**, *527*, 204−210.
(32) *The Elk FP-LAPW Code*, 2009−2012. http://elk.sourceforge.net/ (accessed: October 10, 2011).
(33) Perdew, J. P.; Wang, Y. *Phys. Rev. B* **1992**, *45*, 13244−13249.
(34) Grønvold, F.; Hertzberg, S.; Weeks, O. B.; Schwieter, U.; Paasivirta, J. *Acta Chem. Scand.* **1968**, *22*, 1219−1240.
(35) Schuster, W.; Mikler, H.; Komarek, K. L. *Monatsh. Chem.* **1979**, *110*, 1153−1170.
(36) Margadonna, S.; Takabayashi, Y.; McDonald, M. T.; Kasperkiewicz, K.; Mizuguchi, Y.; Takano, Y.; Fitch, A. N.; Suard, E.; Prassides, K. *Chem. Commun.* **2008**, 5607−5609.
(37) Janaki, J.; Geetha Kumary, T.; Mani, A.; Kalavathi, S.; Reddy, G.; Narasimha Rao, G.; Bharathi, A. *J. Alloys Compd.* **2009**, *486*, 37−41.
(38) Gómez, R. W.; Marquina, V.; Pérez-Mazariego, J. L.; Escamilla, R.; Escudero, R.; Quintana, M.; Hernández-Gómez, J. J.; Ridaura, R.; Marquina, M. L. *J. Supercond. Novel Magn.* **2010**, *23*, 551−557.
(39) Bud'ko, S. L.; Canfield, P. C.; Sefat, A. S.; Sales, B. C.; McGuire, M. A.; Mandrus, D. *Phys. Rev. B* **2009**, *80*, 134523.
(40) McQueen, T. M.; Williams, A. J.; Stephens, P. W.; Tao, J.; Zhu, Y.; Ksenofontov, V.; Casper, F.; Felser, C.; Cava, R. J. *Phys. Rev. Lett.* **2009**, *103*, 057002.
(41) Hamdeh, H. H.; El-Tabey, M. M.; Asmatulu, R.; Ho, J. C.; Huang, T. W.; Yeh, K. W.; Wu, M. K. *EPL (Europhys. Lett.)* **2010**, *89*, 67009.
(42) Ward, J. B.; McCann, V. H. *J. Phys. C: Solid State Phys.* **1979**, *12*, 873−879.
(43) Mizuguchi, Y.; Furubayashi, T.; Deguchi, K.; Tsuda, S.; Yamaguchi, T.; Takano, Y. *Phys. C* **2010**, *470* (Supplement1), S338−S339.
(44) Szymański, K.; Olszewski, W.; Dobrzyński, L.; Satuła, D.; Gawryluk, D. J.; Berkowski, M.; Puźniak, R.; Wiśniewski, A. *Supercond. Sci. Technol.* **2011**, *24*, 105010.
(45) Błachowski, A.; Ruebenbauer, K.; Żukrowski, J.; Przewoźnik, J.; Wojciechowski, K.; Stadnik, Z. *J. Alloys Compd.* **2010**, *494*, 1−4.
(46) Fedorchenko, A. V.; Grechnev, G. E.; Desnenko, V. A.; Panfilov, A. S.; Gnatchenko, S. L.; Tsurkan, V. V.; Deisenhofer, J.; Krug von Nidda, H.; Loidl, A.; Chareev, D. A.; Volkova, O. S.; Vasiliev, A. N. *Low Temp. Phys.* **2011**, *37*, 83−89.